



HAL
open science

Satellite-Based Identification of Large Anthropogenic NMVOC Emission Sources

B Franco, L Clarisse, M van Damme, Juliette Hadji-Lazaro, Cathy Clerbaux,
Pierre-François Coheur

► **To cite this version:**

B Franco, L Clarisse, M van Damme, Juliette Hadji-Lazaro, Cathy Clerbaux, et al.. Satellite-Based Identification of Large Anthropogenic NMVOC Emission Sources. *Journal of Geophysical Research: Atmospheres*, 2024, 129 (22), pp.e2024JD042047. 10.1029/2024jd042047 . hal-04788804

HAL Id: hal-04788804

<https://hal.science/hal-04788804v1>

Submitted on 18 Nov 2024

HAL is a multi-disciplinary open access archive for the deposit and dissemination of scientific research documents, whether they are published or not. The documents may come from teaching and research institutions in France or abroad, or from public or private research centers.

L'archive ouverte pluridisciplinaire **HAL**, est destinée au dépôt et à la diffusion de documents scientifiques de niveau recherche, publiés ou non, émanant des établissements d'enseignement et de recherche français ou étrangers, des laboratoires publics ou privés.



Distributed under a Creative Commons Attribution 4.0 International License



Satellite-Based Identification of Large Anthropogenic NMVOC Emission Sources

Key Points:

- Oversampled IASI satellite data enable the identification of large anthropogenic point sources of CH₃OH, C₂H₂, and C₃H₆ worldwide
- Identified emitters correspond to petrochemistry, coal exploitation, metallurgy, pharmaceutical manufacturing, and megacities
- Combining IASI NMVOC data with inorganic pollutants SO₂ and NH₃ aids in identifying emission sources



Correspondence to:

B. Franco,
bruno.franco@ulb.be

Citation:

Franco, B., Clarisse, L., Van Damme, M., Hadji-Lazaro, J., Clerbaux, C., & Coheur, P. (2024). Satellite-based identification of large anthropogenic NMVOC emission sources. *Journal of Geophysical Research: Atmospheres*, 129, e2024JD042047. <https://doi.org/10.1029/2024JD042047>

Received 24 JUL 2024
Accepted 4 NOV 2024

B. Franco¹ , L. Clarisse¹, M. Van Damme^{1,2}, J. Hadji-Lazaro³, C. Clerbaux^{1,3} , and P. Coheur¹

¹Université libre de Bruxelles (ULB), Spectroscopy, Quantum Chemistry and Atmospheric Remote Sensing (SQUARES), BLU–ULB Space Research Center, Brussels, Belgium, ²Royal Belgian Institute for Space Aeronomy (BIRA–IASB), Brussels, Belgium, ³LATMOS/IPSL, Sorbonne Université, UVSQ, CNRS, Paris, France

Abstract Nonmethane volatile organic compounds (NMVOCs) emitted in excess from anthropogenic sources significantly contribute to the formation of harmful pollutants, thereby degrading air quality. While satellite measurements have become valuable tools for tracking anthropogenic emitters, they have primarily targeted inorganic species and methane (CH₄). This study demonstrates the potential of infrared atmospheric sounding interferometers (IASI) to detect anthropogenic NMVOC point sources on a global scale. Using an advanced oversampling technique, we enhance the spatial resolution of IASI measurements to identify emitters of three major NMVOCs: methanol (CH₃OH), acetylene (C₂H₂), and propylene (C₃H₆). These point sources are primarily associated with chemical and petrochemical facilities, coal-burning activities, metallurgy, pharmaceutical manufacturing sites, and megacities. We also highlight the value of combining IASI measurements of NMVOCs with those of the inorganic species, such as sulfur dioxide (SO₂) and ammonia (NH₃), to aid in the identification of anthropogenic point sources.

Plain Language Summary Human activities release various gases into the atmosphere, including organic (carbon-based) gases, which contribute to the creation of pollutants that can be harmful to both the environment and public health. While satellite measurements increasingly monitor gas emissions from specific human-related sources, they have predominantly focused on inorganic pollutants, like sulfur dioxide (SO₂), ammonia (NH₃), and methane (CH₄). This study explores the potential of satellite observations from infrared atmospheric sounding interferometers (IASI) to detect human-made sources of organic gases globally. Utilizing a specialized technique to increase the spatial resolution of the satellite data, we pinpoint local emitters of three significant organic species: methanol (CH₃OH), acetylene (C₂H₂), and propylene (C₃H₆). These emitters correspond to chemical and petrochemical plants, coal-burning operations, metal production facilities, pharmaceutical manufacturing sites, and large urban areas. Additionally, combining IASI organic gas data with measurements of SO₂ and NH₃ enhances our ability to detect and identify emission point sources.

1. Introduction

Satellite measurements are increasingly used to track anthropogenic emissions of atmospheric pollutants, identifying point sources of nitrogen dioxide (NO₂), sulfur dioxide (SO₂), ammonia (NH₃), and methane (CH₄) (e.g., Beirle et al., 2023; Fioletov et al., 2023; Lauvaux et al., 2022; Van Damme et al., 2018). While global spaceborne studies mainly target these species, nonmethane volatile organic compounds (NMVOCs) from anthropogenic sources raise significant concerns due to their role in forming secondary pollutants like tropospheric ozone (O₃) and particulate matter (Atkinson, 2007; de Gouw et al., 2005; Heald & Kroll, 2020; Volkamer et al., 2006). Elevated NMVOC concentrations in polluted cities and industrialized regions pose air quality challenges, prompting regulatory measures to mitigate emissions. Identifying NMVOC emitters is essential for these efforts. However, due to the limited satellite observations for NMVOCs, investigations into anthropogenic NMVOC emitters have largely been restricted to spaceborne measurements of formaldehyde (HCHO) and glyoxal (CHOCHO) for selected urban sources (e.g., Barkley et al., 2017; Lerot et al., 2021; Zhu et al., 2014; Zuo et al., 2023), or have been constrained by poor spatial coverage by relying on in situ measurements (e.g., Cho et al., 2021; Fried et al., 2020; Parrish et al., 2012; Ryerson et al., 2003; Wert et al., 2003).

Recently, Franco et al. (2022b) leveraged the extensive time series of satellite measurements from the infrared atmospheric sounding interferometer (IASI) to identify over 300 anthropogenic point sources of ethylene (ethene, C₂H₄), a high-yield precursor of HCHO, and tropospheric O₃ (Atkinson, 2007; Fried et al., 2020; Wert

© 2024. The Author(s).

This is an open access article under the terms of the [Creative Commons Attribution-NonCommercial-NoDerivs License](https://creativecommons.org/licenses/by/4.0/), which permits use and distribution in any medium, provided the original work is properly cited, the use is non-commercial and no modifications or adaptations are made.

et al., 2003). Here, we build upon this study to track down anthropogenic emitters of methanol (CH_3OH), acetylene (ethyne, C_2H_2), and propylene (propene, C_3H_6). Along with C_2H_4 , CH_3OH and C_3H_6 are the major building blocks in the modern chemical industry (Yang, 2015), while C_2H_2 is an important precursor of secondary organic aerosol (Volkamer et al., 2009). After introducing the IASI measurements (Section 2.1) and their spatial averaging (Section 2.2), we provide spectral evidence of the first identification from space of these compounds in the plumes from large industrial facilities (Section 2.3). Subsequently, we report and categorize the detected emitters (Section 3). Finally, we demonstrate the potential of infrared satellite measurements of NMVOCs to complement those of inorganic pollutants (NH_3 and SO_2), thereby enhancing our understanding of anthropogenic emitters (Section 4), before presenting an outlook (Section 5).

2. Data and Methods

2.1. Satellite Measurements

Deployed on board the polar-orbiting European meteorological satellites (Metop), IASI measures the Earth-atmosphere outgoing radiance across the thermal infrared ($645\text{--}2,760\text{ cm}^{-1}$), achieving global coverage twice daily (Clerbaux et al., 2009). Here, we utilize the entire observational time series from IASI/Metop-A (2007–2021), -B (2013–2023), and -C (2019–2023), discarding cloudy scenes and nighttime measurements, which typically exhibit reduced sensitivity due to the lower thermal contrast (Di Gioacchino et al., 2024). The resulting multiyear data set comprises over 1.9×10^9 measurements.

In recent years, the development of the hyperspectral range index (HRI) has played a pivotal role in improving the detection of weak infrared absorbers with IASI (e.g., Clarisse, Clerbaux, et al., 2019; Clarisse, Franco, et al., 2023; Franco, Clarisse, Theys, et al., 2024; Franco et al., 2018). The HRI quantifies the strength of spectral absorption attributed to a trace gas by aggregating the contributions from all spectral bands in which this species is absorbs (Clarisse et al., 2013; Walker et al., 2011). Following the procedure detailed by Franco et al. (2018), we constructed an HRI for each trace gas targeted in this study, using the following wave number ranges: $960\text{--}1,080\text{ cm}^{-1}$ for CH_3OH , $725\text{--}735\text{ cm}^{-1}$ for C_2H_2 , and $905\text{--}920\text{ cm}^{-1}$ for C_3H_6 . As described by Clarisse, Franco, et al. (2023), the covariance matrix used for setting up the C_2H_2 HRI accounts for long-term changes in carbon dioxide (CO_2), a major interference in the $725\text{--}735\text{ cm}^{-1}$ range. Additionally, we excluded the 10, 1, and 2 smallest eigenvalues of that matrix for CH_3OH , C_2H_2 , and C_3H_6 , respectively, to avoid artifacts caused by instrument calibration or postprocessing in the IASI time series (Clarisse, Franco, et al., 2023). An HRI value was then calculated for each IASI observation and for each species.

The long-term alignment of the IASI-A, -B, and -C instruments have been evaluated, showing that the instruments are stable and consistent during their overlapping years (Bouillon et al., 2020; Saunders et al., 2021). Moreover, the HRI values for the different NMVOCs over remote regions are consistently close to zero, as expected when there is no detectable trace gas (Clarisse et al., 2013). These assessments provide confidence that no significant systematic differences exist between the IASI instruments in detecting trace gases.

2.2. Supersampling

Oversampling techniques have become commonly used to track down emission point sources of atmospheric pollutants (e.g., Sun et al., 2018; Zhu et al., 2014). By combining multiple satellite observations of a given scene, oversampling capitalizes on the partial overlap among the varying measurement footprints to yield information at a higher spatial resolution than the sounder's native resolution. This process produces high-resolution gas distributions that unveil localized geographical features corresponding to pollutant hotspots.

We have applied an augmented version of oversampling developed by Clarisse, Van Damme et al. (2019b), termed hereafter as supersampling, to the IASI HRI data sets. This method integrates two key concepts:

- **Wind rotation:** This involves rotating each satellite observation around a presumed gas emitter according to the daily horizontal wind direction, aligning all the measurements in the same direction (e.g., Beirle et al., 2011; Valin et al., 2013). The result is a measurement distribution in which the winds blow in a uniform direction, enhancing the representation of the gas emitter and its plume (downwind average) while mitigating contributions from nearby sources. Here, the daily horizontal wind fields are sourced from the European

Center for Medium-Range Weather Forecasts (ECMWF) ERA5 reanalysis (Hersbach et al., 2020) and collocated with the IASI measurements.

- Super-resolution: Applied to satellite measurements, it consists of repeating the oversampling procedure and correcting the resulting oversampled average at each step until the produced average distribution achieves full consistency with the satellite data (Clarisse, Van Damme et al., 2019b). Wind adjustment preceding each step ensures the homogeneity of the underlying satellite data distribution throughout the process. The wind-adjusted, super-resolved distribution provides a more realistic representation of hotspot strengths and resolves much finer spatial features, thereby significantly enhancing IASI's detection capabilities.

Wind rotation assumes prior knowledge of the potential gas emitter locations. However, such information is often limited or unavailable, especially for NMVOCs. Therefore, we adopted the method described by Clarisse, Van Damme et al. (2019b), which consists of creating a world map at a hyperfine spatial resolution ($0.01^\circ \times 0.01^\circ$) and treating each grid cell as a presumed emitter. For each grid cell, supersampling is applied to the entire IASI HRI data set, using the grid cell center as the point of wind rotation. From the resultant wind-adjusted, super-resolved distribution, an average HRI value over the downwind area of the presumed emitter is computed and assigned to that grid cell. This process is repeated for each grid cell and for each of the target species independently. Ultimately, we obtained a 2007–2023-averaged $0.01^\circ \times 0.01^\circ$ global distribution for each compound (Figure A1 of Appendix A). The supersampled distribution enables the detection of hotspots that might be challenging or impossible to discern with oversampling alone (Clarisse, Van Damme et al., 2019b; Franco et al., 2022b). The examples of NMVOC hotspots in Figures 1, 4 and 5 are zoom-ins from the global distributions obtained with supersampling.

A significant advantage of using the HRI instead of retrieved gas vertical column densities (VCDs) for supersampling is that it conveys the cumulative information on the target gas present in the satellite spectra and is primarily affected only by instrumental noise (Clarisse et al., 2013; Whitburn et al., 2016). In contrast, VCDs are influenced by additional uncertainties resulting from the HRI-to-VCD conversion, including errors inherited from variables describing the atmosphere and the surface. Due to the weak absorptions of NMVOCs in the thermal infrared, the advantage provided by the HRI is crucial for detecting point sources. As demonstrated by Franco et al. (2022b), utilizing the HRI unveiled C_2H_4 point sources that would have otherwise gone undetected with retrieved VCDs.

The supersampled global distributions of CH_3OH , C_2H_2 , and C_3H_6 (Franco, Clarisse, & Coheur, 2024) exhibit variable backgrounds (Figure A1 of Appendix A). Elevated HRI values of CH_3OH and C_2H_2 primarily reflect their regional sources, with substantial contributions from biogenic sources for CH_3OH , Northern Hemisphere biofuel combustion for C_2H_2 , and biomass burning for both compounds. The relatively high, homogeneous C_2H_2 background is due to its longer atmospheric lifetime (~ 2 weeks; Xiao et al., 2007), which enables its long-range transport and mixing in the troposphere. Conversely, the short C_3H_6 lifetime against reactions with the hydroxyl radical (OH) and O_3 (a few hours–1.5 days; Atkinson & Arey, 2003; Seinfeld & Pandis, 2016) results in low background HRI values. Enhancements over deserts are attributed to surface emissivity artifacts (Clarisse, Clerbaux, et al., 2019; Franco et al., 2022b), particularly affecting the C_3H_6 spectral absorption band (Zhou et al., 2011).

Zoom-ins of specific regions in these distributions reveal pronounced local HRI enhancements of 20–40 km geographical extent, corresponding to emission hotspots. Due to varying observational conditions and the presence of false positives (e.g., surface emissivity effects or frequent wildfires), the hotspot identification was based on a careful manual inspection of the data, using two main criteria: a significant local HRI enhancement, clearly differentiating from the surrounding background and the presence of anthropogenic activities (e.g., industrial or urban areas) at the location, as confirmed by visible satellite imagery. It has been demonstrated by Clarisse, Van Damme et al. (2019b) that the gas emitter(s) can be found with supersampling within a distance of 5 km from the local HRI maximum for most point sources. Figure 1 illustrates a typical hotspot for each compound. Close-up views with satellite visible imagery reveal potential emitters, such as chemical plants in the Ningdong Industrial Park (Ningxia, China) for CH_3OH , coal processing plants near Wuhai (Inner Mongolia, China) for C_2H_2 , and the Secunda petrochemical complex (South Africa) for C_3H_6 (Figure 1). Each example suggests that the gas enhancements detected with IASI can be traced back to emissions from heavy industrial activities. Interestingly, these sites have also been identified as anthropogenic point sources of C_2H_4 by Franco et al. (2022b), as shown in Figure 1. C_2H_4 industrial emitters have been associated with chemical and petrochemical clusters, iron and steel plants, and various coal-related industries.

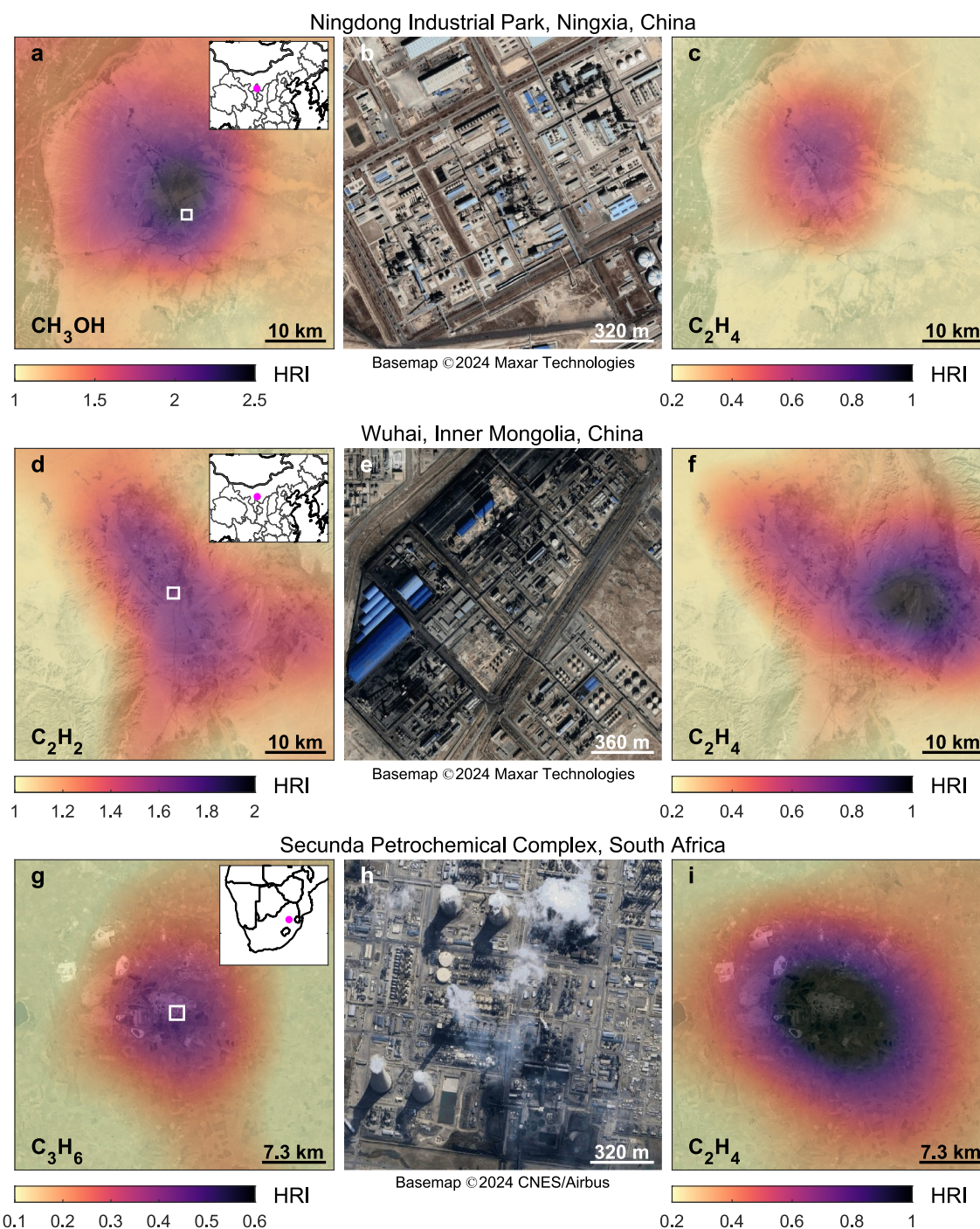


Figure 1. 2007–2023 averaged $0.01^\circ \times 0.01^\circ$ IASI HRI for CH_3OH (a), C_2H_2 (d), and C_3H_6 (g) around hotspot examples, obtained by wind-rotated supersampling. The white squares indicate the location of the source emitter(s) and correspond to the close-up views in (b, e, and h) with satellite visible imagery. (c, f, i) Supersampling of the 2007–2023 averaged IASI C_2H_4 HRI at a $0.01^\circ \times 0.01^\circ$ spatial resolution, at the locations of the CH_3OH , C_2H_2 , and C_3H_6 hotspots.

2.3. Spectral Evidence

Despite its high sensitivity, the HRI is prone to false detections when the spectral signature of another trace gas or of surface emissivity overlap and resemble that of the target species. In this section, we provide spectral evidence that CH_3OH , C_2H_2 , and C_3H_6 significantly contribute to the HRI enhancements identified as hotspots. To this end, we applied the whitening transformation of spectra introduced by De Longueville et al. (2021) to IASI

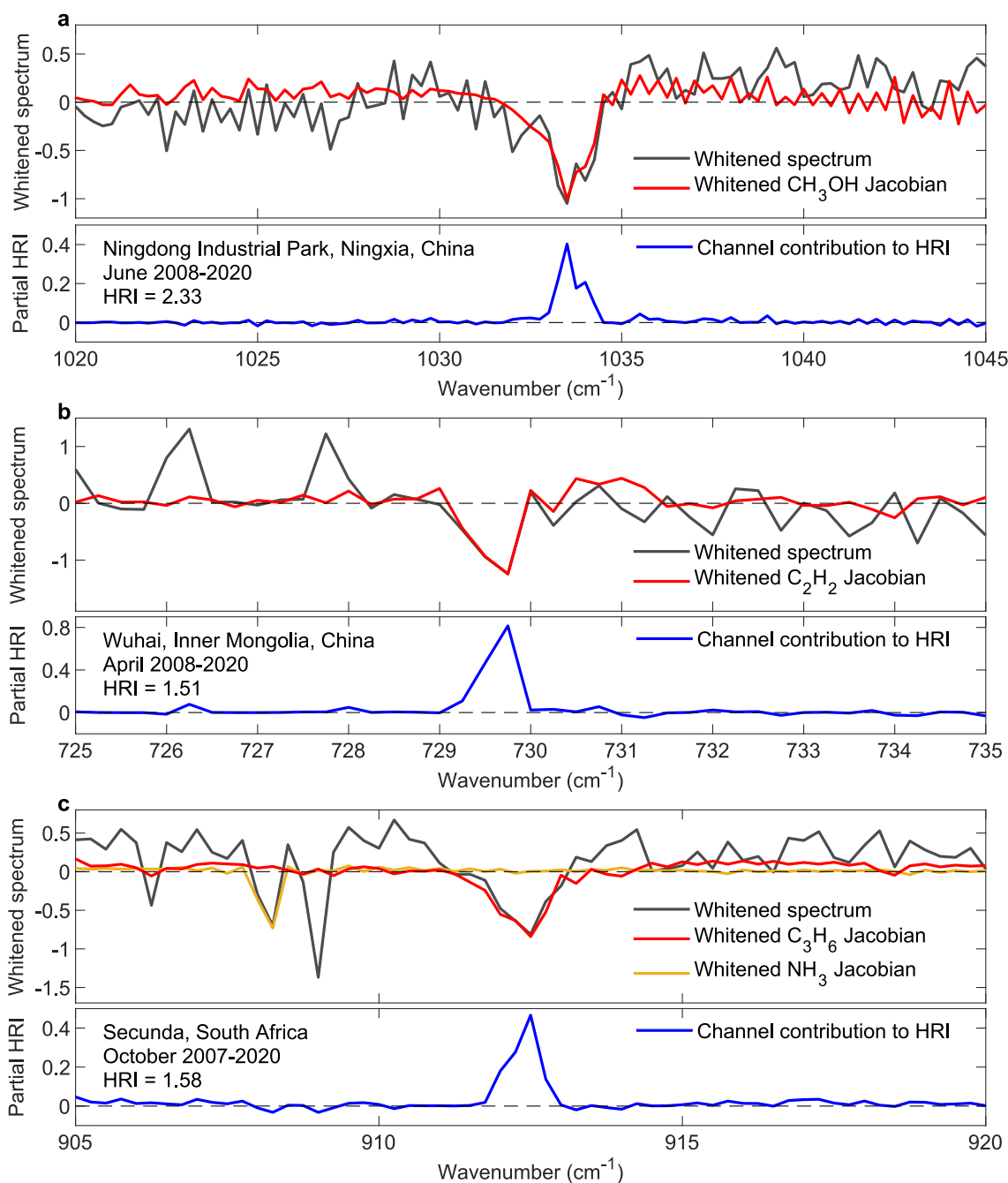


Figure 2. Results of the whitening transformation (in gray) applied to averaged IASI spectra taken over CH_3OH (a), C_2H_2 (b), and C_3H_6 (c) hotspots. Whitened Jacobians for the target species (in red), potential interfering gases (in yellow), and contribution of each spectral channel to the HRI (in blue). Other major spectral residuals correspond to water vapor. Both y-axes are unitless.

observations over detected hotspots. Examples are displayed in Figure 2 for the point sources presented in Figure 1. For each hotspot, we selected a month with favorable observational conditions and averaged all IASI/Metop-A spectra with an HRI value of the target compound greater than 1 for that month throughout the 2007–2020 time series before applying the whitening transformation to these averaged spectra.

The whitening transformation produces a spectrum where all spectral absorptions deviating from the climatological normality are highlighted (gray curves in Figure 2). After applying the whitening to the averaged IASI spectra, we observe in Figure 2 strong spectral residuals that closely match the whitened spectral signature (the

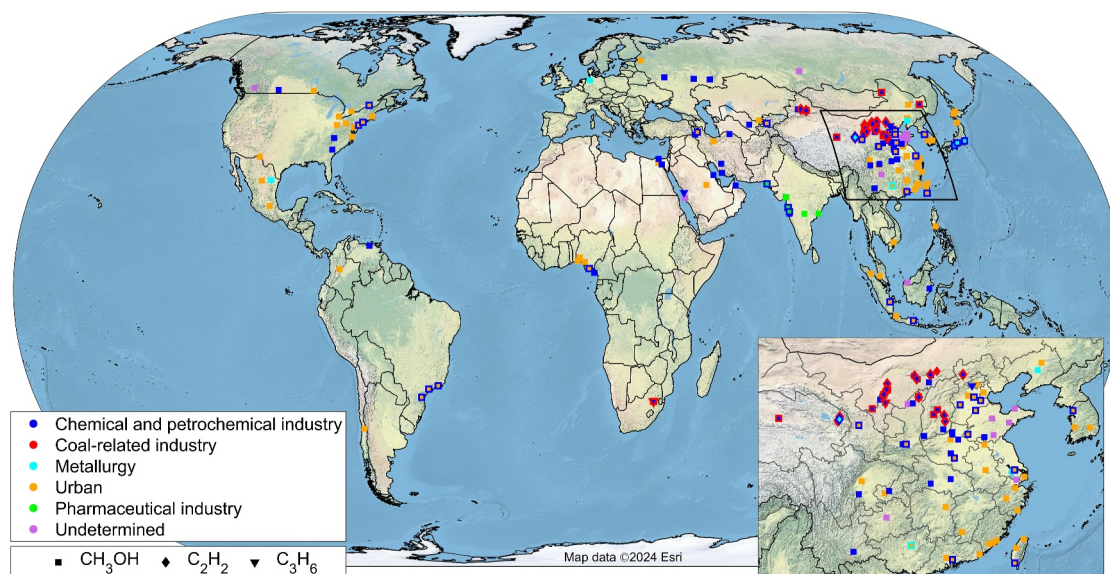


Figure 3. Global distribution of CH_3OH , C_2H_2 , and C_3H_6 point sources detected by IASI and their categorization. In cases where a hotspot falls into multiple categories, only the two main categories are shown on the map.

Jacobian) of the target species in each example (red curves). This provides firm evidence that the elevated HRI values observed over the hotspots correspond to actual enhancements of CH_3OH , C_2H_2 , and C_3H_6 . Additionally, as shown by Franco et al. (2022b) and Franco, Clarisse, Theys, et al. (2024) for both individual and averaged spectra, element-wise multiplication of the whitened spectrum and target gas's Jacobians quantifies the contribution of each spectral channel to the HRI calculated over the entire spectral range (visualized as blue curves in Figure 2). For the three target species, the spectral channels contributing to the HRI correspond exactly to their main absorption features, while contributions from other channels are negligible. For instance, the spectral residual identified at 908 cm^{-1} in the C_3H_6 spectral range (Figure 2c), attributed to NH_3 , does not contribute as it is nullified by the C_3H_6 Jacobian. This analysis demonstrates that the CH_3OH , C_2H_2 , and C_3H_6 hotspots identified with IASI can be unequivocally attributed to industrial point sources.

3. Results

We conducted a systematic analysis of the supersampled maps of CH_3OH , C_2H_2 , and C_3H_6 to identify gas hotspots worldwide. For each detected hotspot, we used satellite visible imagery and online data regarding the types of companies and industrial activities in the area to determine the likely gas emitter(s). We report in Figure 3 the global distribution of all NMVOC hotspots detected with IASI, categorized by the type of identified emitters. A total of 157 CH_3OH hotspots, 16 C_2H_2 hotspots, and 4 C_3H_6 hotspots were detected (Franco, Clarisse, & Coheur, 2024), with a predominant concentration in the Northern Hemisphere, particularly in East Asia. These hotspots, listed in Tables A1–A3 of Appendix A, correspond to five main types of sectoral emissions: chemical and petrochemical industry, coal-related industry, metallurgy, pharmaceutical industry, and urban areas. In some cases, identifying a distinct emitter was not possible. A single hotspot may also originate from multiple nearby point sources of various types. In these instances, only the two predominant categories are depicted in Figure 3.

It is worth noting that the point sources identified with IASI do not exclusively represent the largest global emitters of these NMVOC compounds. While emission strength is a key factor influencing detection, several other elements come into play. In regions with dense populations and industrial activities, elevated background levels of NMVOCs and the proximity of multiple emitters can obscure individual sources, making distinct hotspot detection more challenging. Furthermore, poor observational conditions—such as weak thermal contrast or frequent cloud cover—can prevent even significant emitters from being detected.

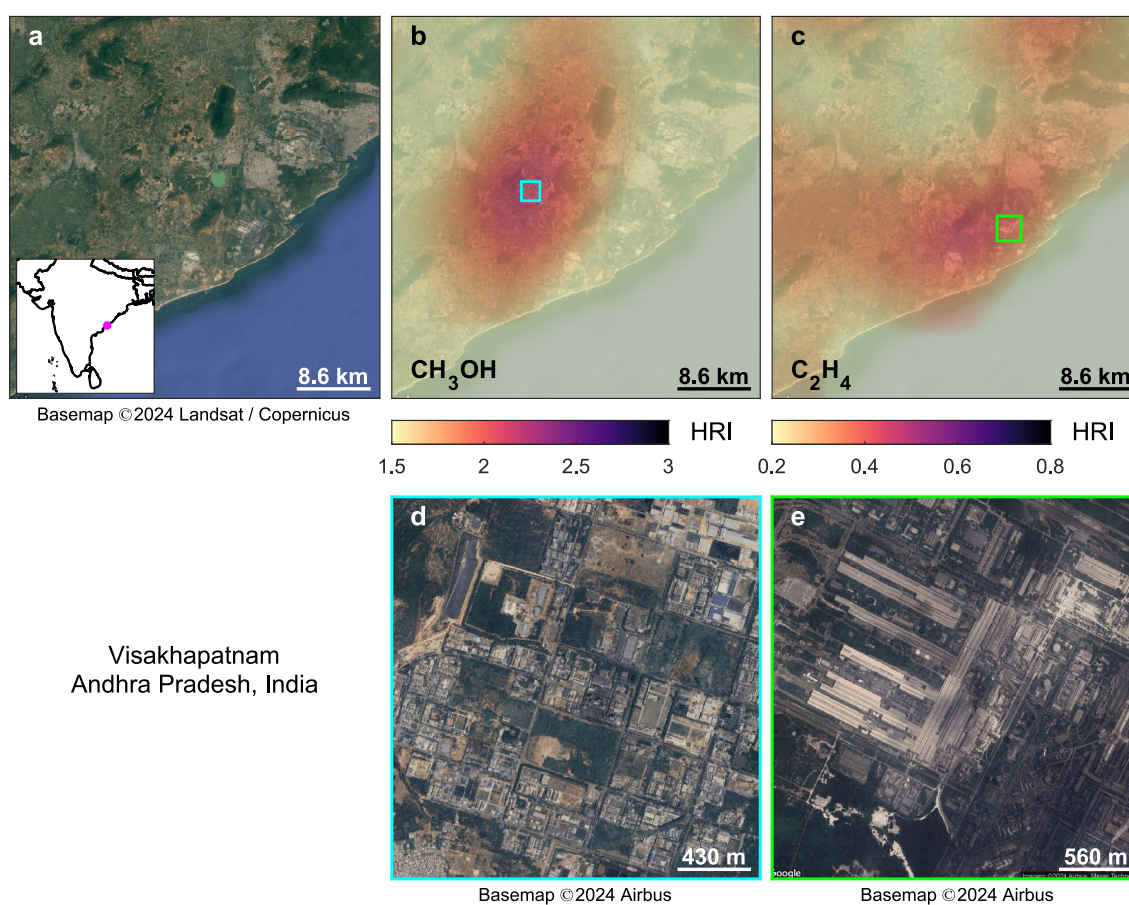


Figure 4. Visible satellite imagery (a), and 2007–2023 averaged $0.01^\circ \times 0.01^\circ$ IASI HRI of CH_3OH (b) and C_2H_4 (c) obtained by wind-rotated supersampling, over Visakhapatnam, Andhra Pradesh, India. The colored squares indicate the locations of the emission sources, corresponding to the close-up views of the CH_3OH and C_2H_4 point source emitters: the Jawaharlal Nehru Pharma City (d) and the Vizag Steel Plant (e), respectively.

3.1. C_3H_6 Point Sources

C_3H_6 has been detected previously with IASI during the exceptional 2009 and 2019/2020 Australian bushfires (Clarisse, R'Honi et al., 2011; De Longueville et al., 2021). With the identification of four C_3H_6 point sources, we present the first detection of anthropogenic C_3H_6 from space (Figure 3). They correspond to Secunda (South Africa), Rabigh (Saudi Arabia), Ningdong base, and Fangshan District (China). The fact that only four large emitters are detected is likely explained by the high reactivity of C_3H_6 in the low troposphere and its weak spectral absorption. These point sources are associated with major petrochemical clusters, which are also sites of C_2H_4 emissions (Franco et al., 2022b).

With a global production of $\sim 120 \text{ Mt yr}^{-1}$, C_3H_6 serves—along with C_2H_4 ($\sim 190 \text{ Mt yr}^{-1}$)—as a primary building block for plastics, fibers, and various other chemicals (Zimmermann, 2013; Zimmermann & Walzl, 2009). C_3H_6 is produced industrially through steam cracking of hydrocarbons (ethane, propane, and naphtha) and as a by-product of crude oil refining. Emissions of C_3H_6 can therefore occur from petrochemical facilities during its production and processing, from stack flaring, or through leaks and accidental releases. Substantial amounts have indeed been measured in situ in industrial plumes downwind of petrochemical complexes similar to those identified with IASI (Cho et al., 2021; Fried et al., 2020; Parrish et al., 2012; Ryerson et al., 2003; Wert et al., 2003).

Two of the four identified C_3H_6 point sources are also characterized by coal mining and processing activities, like at Secunda (Figure 1). In regions where oil and gas reserves are limited or too expensive to exploit, coal-to-olefins (CTO) and methanol-to-olefins (MTO) conversion technologies have emerged as substitutes to the conventional production pathways (Amghizar et al., 2017; Zimmermann, 2013; Zimmermann & Walzl, 2009). In the CTO

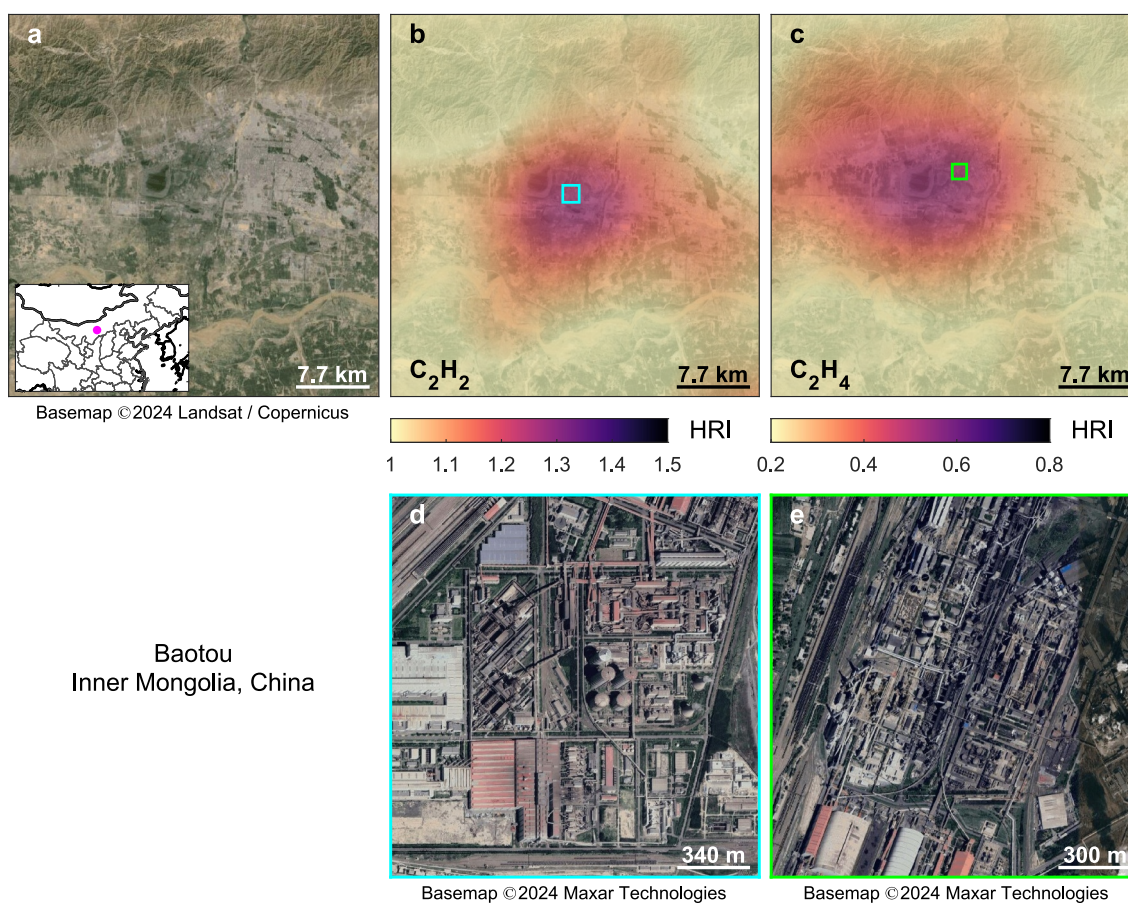


Figure 5. Visible satellite imagery (a), and 2007–2023 averaged $0.01^\circ \times 0.01^\circ$ IASI HRI of C_2H_2 (b) and C_2H_4 (c) obtained by wind-rotated supersampling, over Baotou, Inner Mongolia, China. The colored squares indicate the locations of the emission sources, corresponding to the close-up views of the C_2H_2 and C_2H_4 point source emitters (d–e).

process, coal is gasified to produce synthesis gas (syngas), a mixture of carbon monoxide and hydrogen, which serves as feedstock for the production of fuels and chemicals, including light olefins (C_2H_4 and C_3H_6), CH_3OH , and NH_3 . In the MTO route, CH_3OH itself is converted by dehydration into light olefins. In point sources where coal is used as raw material, C_3H_6 released from the incomplete heating and burning of coal adds to the emissions from chemical facilities.

3.2. CH_3OH Point Sources

While available spaceborne observations of CH_3OH primarily relate to its biogenic sources (e.g., Cady-Pereira et al., 2012; Franco et al., 2018; Wells et al., 2012), here we identify anthropogenic CH_3OH emissions by detecting 157 global point sources from space, with most located in Asia, the Middle East, and eastern North America (Figure 3). Although CH_3OH can be produced from atmospheric gas precursors (Bates et al., 2021; Jacob et al., 2005; Millet et al., 2008; Müller et al., 2016), this secondary formation primarily affects the CH_3OH background and is assumed to have little impact on the local enhancements detected by IASI over point sources.

Global industrial production of CH_3OH amounts to 90–100 Mt yr^{-1} , positioning it—after C_2H_4 and C_3H_6 —as the third most abundantly produced organic compound (Ott et al., 2012; Yang, 2015). CH_3OH is generally obtained by catalytic conversion of syngas, and roughly 85% of synthesized CH_3OH is utilized directly in the chemical industry as feedstock or solvent (Ott et al., 2012). It is therefore no surprise that half of the CH_3OH point sources are associated with chemical and petrochemical facilities (e.g., in the Middle East). The industrial synthesis of CH_3OH is increasingly used as a substitute for petroleum products, particularly via the CTO/MTO pathways

(Zimmermann, 2013; Zimmermann & Walzl, 2009), which explains why many of the CH_3OH point sources associated with chemical facilities are also characterized by coal refining (Figure 3).

Some CH_3OH hotspots are found over areas hosting a cluster of pharmaceutical companies, laboratories, and manufacturing facilities, known as pharma cities, especially in India (Figure 3). A typical example is the CH_3OH point source associated with the Jawaharlal Nehru Pharma City, west of Visakhapatnam, India (Figure 4). CH_3OH serves indeed as a solvent and starting material for the synthesis of various medicines and pharmaceutical intermediates (Ott et al., 2012). Among the current satellite products, CH_3OH is the only species that allows pinpointing specifically to this industrial sector. The area of this CH_3OH point source is also the site of a significant, eastward-shifted C_2H_4 enhancement (Figure 4c), attributed to emissions from an integrated steel plant (Franco et al., 2022b).

The remaining CH_3OH point sources are associated with megacities such as Tianjin, Jakarta, and Lagos (Figure 3). Elevated concentrations of CH_3OH have been measured in dense urban environments (e.g., de Gouw et al., 2018; Simpson et al., 2020) due to its use in the fuel and energy sector. Incomplete combustion, for example, from vehicle exhaust and domestic heating, can also release CH_3OH . As explained by Franco et al. (2022b), urban point sources are generally more difficult to detect from space because the associated emissions are more diffuse than for industrial sources. Furthermore, urban and industrial CH_3OH emissions cannot be distinguished when heavy industries are located in urban areas. For instance, the cities Rio de Janeiro, Sao Paulo, and Curitiba (Brazil), which emerge as local emitters, host petrochemical hubs.

3.3. C_2H_2 Point Sources

Spaceborne measurements of C_2H_2 indicate a significant influence from biomass burning regions and a notable latitudinal gradient due to prevalent anthropogenic sources in the Northern Hemisphere (Bernath et al., 2020; Duflot et al., 2015). Given its longer lifetime of ~ 2 weeks (Xiao et al., 2007), the supersampled IASI C_2H_2 distribution exhibits a higher HRI background compared to CH_3OH (4–7 days; Bates et al., 2021; Khan et al., 2014; Müller et al., 2016), C_3H_6 , and C_2H_4 (both with lifetimes ranging from a few hours to 1.5 days; Atkinson & Arey, 2003; Seinfeld & Pandis, 2016), resulting in weaker and more diffuse C_2H_2 hotspots that are challenging to detect. We have, however, identified 16 C_2H_2 point sources, all of which are associated with a heavy industry (Figure 3).

Before the emergence of the cheaper, more competitive light olefins, C_2H_2 was a key building block in industrial organic chemistry due to its capacity to be converted into valuable products with high yields (Pässler et al., 2011). Although its industrial production—primarily through steam cracking of hydrocarbons—has steadily declined, C_2H_2 remains utilized in the chemical industry, particularly for synthesizing vinyl compounds, as well as in metal processing. China currently stands as the largest producer of C_2H_2 and consumes $\sim 80\%$ of the global production (Pässler et al., 2011). Noteworthy, all the C_2H_2 point sources identified with IASI are in China (Figure 3), predominantly concentrated in the northern central provinces (e.g., Inner Mongolia, Ningxia, and Shanxi).

The C_2H_2 point sources are characterized by chemical industries, coal-related activities, and metallurgy. Similar to C_3H_6 and CH_3OH , C_2H_2 emissions from chemical facilities can occur through gas flaring and fugitive releases. As a by-product of pyrolytic reactions, C_2H_2 is also emitted from the incomplete combustion of hydrocarbons, from the incomplete gasification of coal during the production of syngas, and from coal undergoing high-temperature pyrolysis to produce coke in the iron and steel industry (Pässler et al., 2011). The majority of these point sources are common to both C_2H_2 and C_2H_4 (Franco et al., 2022b), such as Baotou, Inner Mongolia, which gathers coal mining and processing activities, coal-fired power plants, steel plants, and chemical industries (Figure 5).

4. Case Study

Identifying point sources is often challenging due to the presence of various potential emitters at the same location, especially in regions where information is sparse or difficult to obtain. Combining organic and inorganic tracers to study anthropogenic emissions can provide more insights into largest gas emitters and help identify the most polluted areas for further dedicated measurements. As a case study, we analyze the supersampled distributions of C_2H_2 , C_2H_4 , C_3H_6 , and CH_3OH , as well as those of SO_2 HRI and NH_3 VCDs from IASI (Clarisse, Van Damme et al., 2019b; Van Damme et al., 2018), depicted as contour plots in Figure 6, over an industrial valley in the Inner Mongolia and Ningxia provinces (China).

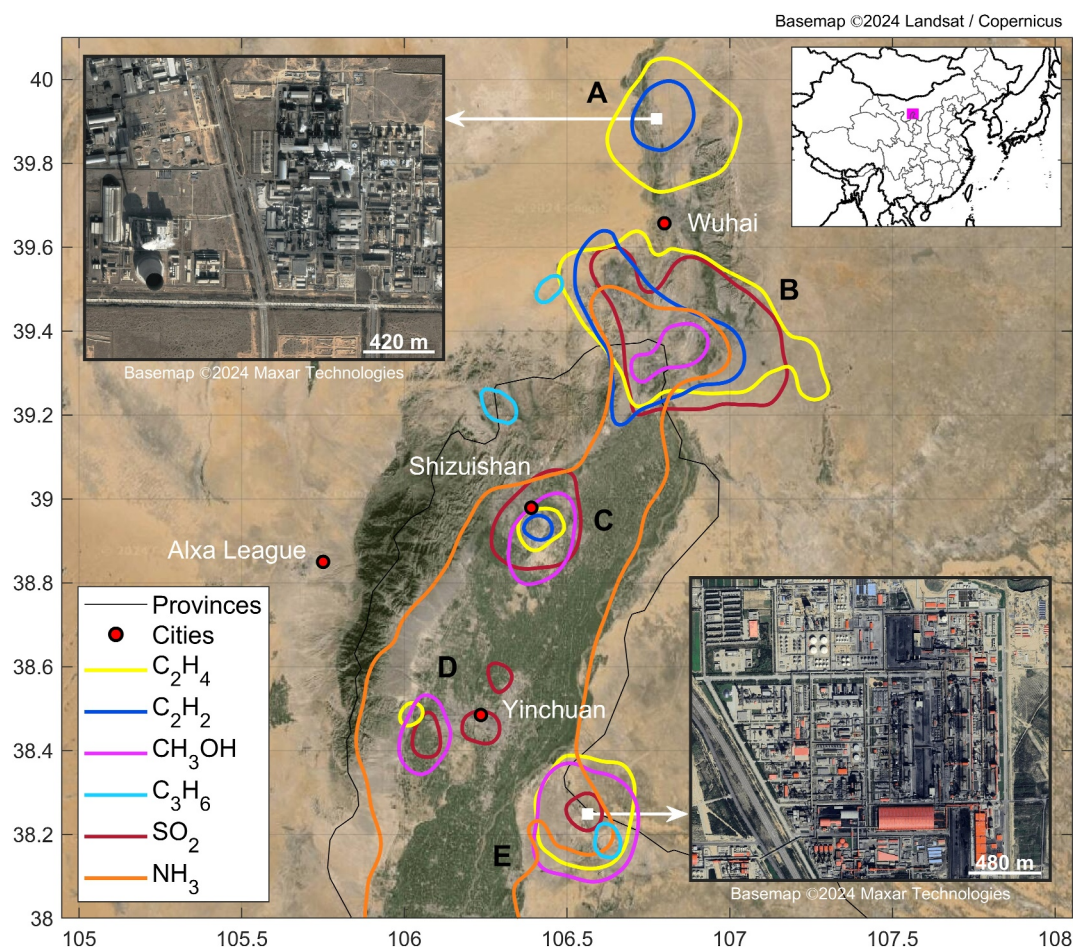


Figure 6. Clustered point sources of atmospheric pollutants detected by IASI in an industrial valley in central China. Hotspots are outlined by colored contour lines representing C_2H_4 HRI = 0.4, C_2H_2 HRI = 1.2, CH_3OH HRI = 1.5, C_3H_6 HRI = 0.3, SO_2 HRI = 2.5, and NH_3 column = 1.5×10^{16} molec cm^{-2} , obtained from the supersampled distribution of each species. Insets present zoom-ins of potential emitters.

Although there is a much longer history of measuring anthropogenic SO_2 emissions using ultraviolet-visible satellite sounders (e.g., Fioletov et al., 2013; Fioletov et al., 2023; Liu et al., 2018; McLinden et al., 2016; Theys et al., 2021) compared to infrared instruments (e.g., Clarisse, Fromm, et al., 2011), and despite the lower sensitivity of thermal infrared measurements to SO_2 in the lowermost atmospheric layers due to the weak thermal contrast between the surface and the boundary layer, we make use of IASI SO_2 data to maintain consistency in spatial resolution, footprint, overpass time, and vertical sensitivity with the NMVOCs and NH_3 measurements. Note that in Figure 6, results for NH_3 are expressed in VCDs.

These distributions reveal a significant cluster of gas hotspots, delineated with a constant HRI (or VCD) threshold specific to each compound in Figure 6: C_2H_4 HRI = 0.4, C_2H_2 HRI = 1.2, CH_3OH HRI = 1.5, C_3H_6 HRI = 0.3, SO_2 HRI = 2.5, and NH_3 column = 1.5×10^{16} molec cm^{-2} . These thresholds were selected to clearly visualize the gas hotspots in this case study and vary by species and region depending on local background gas concentrations and observational conditions, particularly thermal contrast. The gas hotspots are concentrated around five locations (labeled A–E), each corresponding to the point source of at least two different species and hosting a high density of industrial facilities. Coal-related activities are particularly prevalent in the region, as coal has been the primary feedstock supporting industrial and economic development in central China (Crelling et al., 2010; Li et al., 2019; Tong et al., 2018).

Location B exhibits significant enhancements in all species (except C_3H_6), indicating that large gas releases can occur from the many coal mines, coke plants, and coal-fired power plants in the area. CH_3OH enhancement in the

absence of large cities suggests additional emissions from chemical plants, contributing to the C_2H_2 and C_2H_4 hotspots. Conversely, CH_3OH and C_2H_4 enhancements at locations C–D may primarily be attributed to the urban agglomeration, while C_2H_2 and SO_2 hotspots would indicate emissions from coal refining facilities, power plants, and steel factories. A large chemical complex could be responsible for CH_3OH , C_2H_4 , and C_3H_6 fluxes at location E. In particular, the C_3H_6 point source, confirmed through spectral analysis, corresponds to an olefin plant. Two other spots with C_3H_6 HRI above the defined threshold are observed in the region, but those are false detections due to spectral emissivity anomalies from rocks and sands. Metallurgy activities, likely smelters, are also present and can release SO_2 at location E. Conversely, the northernmost location A exhibits C_2H_2 and C_2H_4 hotspots only, likely due to the coal sector. In contrast to other species, NH_3 shows substantial enhancement covering a large part of the area, attributable to agriculture and husbandry activities throughout the valley. Chemical industries also contribute at locations B and E due to the presence of fertilizer plants (Clarisse, Van Damme et al., 2019b; Van Damme et al., 2018).

5. Outlook

This study demonstrates the feasibility of detecting anthropogenic emission point sources of small (NM)VOCs using infrared satellite data. It represents a significant step toward future endeavors, which might include inferring top-down emission fluxes from identified point sources. This would be of particular interest as top-down estimates derived from time-resolved airborne observations are tailored to specific sites, whereas satellite data sets provide the means to infer emissions from global point sources using a single sounder. Additionally, spaceborne fluxes of inorganic species have already shown that current bottom-up emission inventories often misrepresent these point sources and their emission rates (e.g., Beirle et al., 2023; Fioletov et al., 2023; Van Damme et al., 2018). Similarly, inferring top-down fluxes of NMVOCs will be essential for improving our understanding and representation of anthropogenic emissions.

The weak spectral absorption of NMVOCs, leading to high uncertainties in retrieved VCDs, currently hinders this task. However, our study serves as a proof of concept in light of forthcoming infrared satellite sounders, including the polar-orbiting IASI-New Generation (IASI-NG) and the geostationary Infrared Sounder on board Meteosat Third Generation (MTG-IRS). With enhanced instrumental performance compared to IASI, or with extensive spatial coverage and up to 30-min revisit times, these future sounders are anticipated to detect a greater number of anthropogenic emitters and provide the potential for top-down quantification of their emission rates.

Appendix A: Supplementary Materials

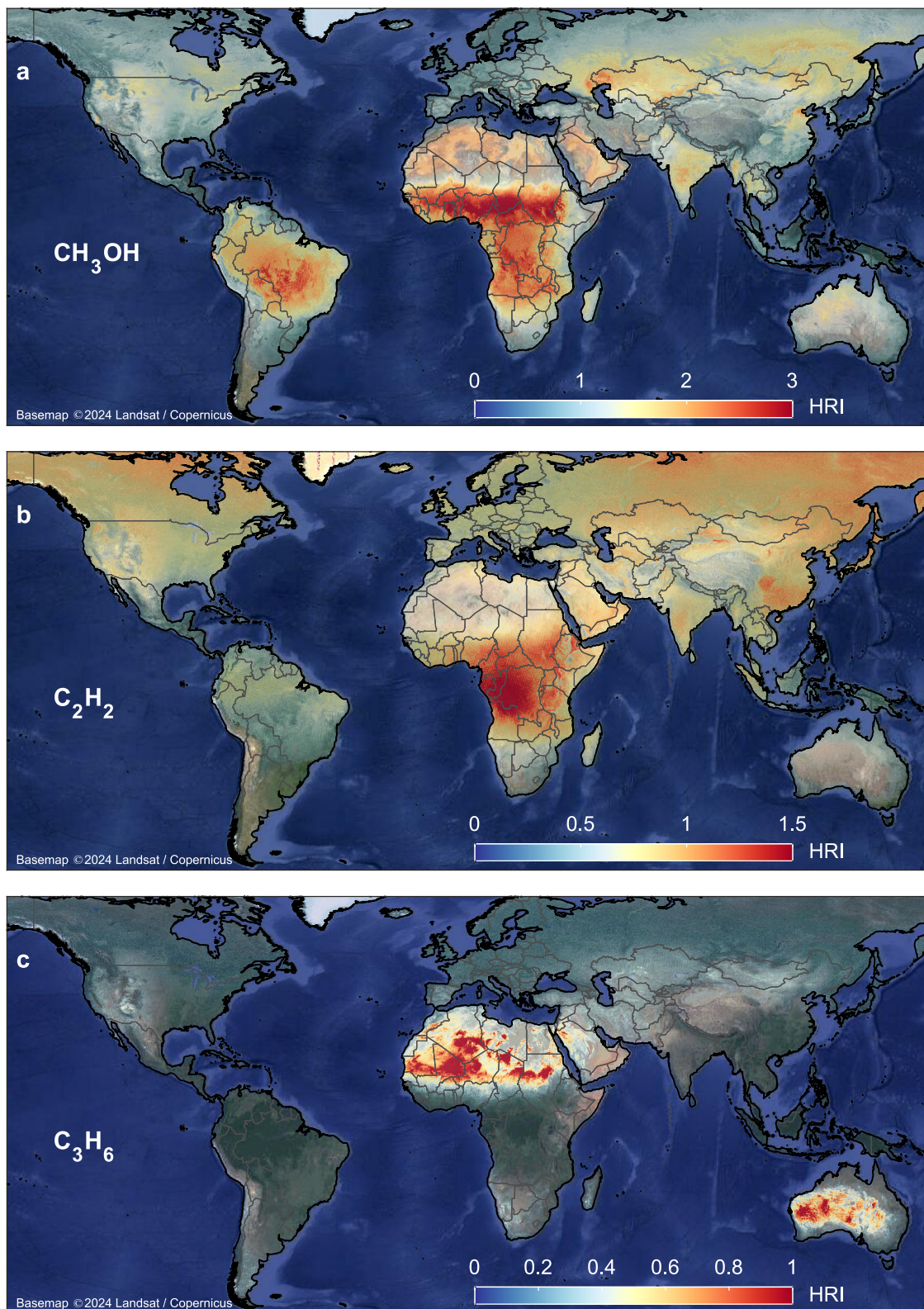


Figure A1. 2007–2023 averaged $0.01^\circ \times 0.01^\circ$ global distribution of CH_3OH (a), C_2H_2 (b), and C_3H_6 (c) HRI, obtained by wind-rotated supersampling of the IASI data. The C_3H_6 HRI enhancements observed over deserts (e.g., Sahara and Australia) are due to surface emissivity anomalies.

Table A1
A Catalog of CH₃OH Point Sources, With Identified Potential Emitters

	Name	Country	Lat	Lon	Ch	Co	Me	Ur	Ph	Un
1	Curitiba	Brazil	-25.516	-49.348	x			x		
2	Rio de Janeiro	Brazil	-22.719	-43.408	x			x		
3	Sao Paulo	Brazil	-23.527	-46.652	x			x		
4	Kamloops	Canada	50.693	-120.407						x
5	Medicine Hat	Canada	50.080	-110.664	x					
6	Montreal	Canada	45.547	-73.677	x			x		
7	Toronto	Canada	43.755	-79.399				x		
8	Winnipeg	Canada	49.841	-97.107				x		
9	Santiago	Chile	-33.473	-70.762				x		
10	Anshan	China	41.152	122.912			x	x		
11	Anyang	China	36.106	114.214			x			
12	Baise	China	23.739	106.871		x				x
13	Baoding	China	38.834	115.462				x		
14	Baotou	China	40.614	109.690	x		x			
15	Beijing	China	39.845	116.421				x		
16	Cangzhou	China	38.388	116.815	x			x		
17	Changsha	China	28.190	113.058				x		
18	Changshou District	China	29.776	107.008	x		x			
19	Changzhou	China	31.697	120.168			x	x		
20	Chengdu	China	30.742	104.068				x		
21	Chongqing	China	29.572	106.533				x		
22	Dalad Banner	China	40.321	110.060	x					
23	Dezhou	China	37.468	116.278	x			x		
24	Dongguan	China	22.932	113.805	x			x		
25	Gaomi City	China	36.334	119.858						x
26	Guangzhou/Foshan	China	23.120	113.122				x		
27	Hainan District	China	39.370	106.856	x	x				
28	Hamusi Golmud	China	36.729	95.202	x	x				
29	Harbin	China	45.681	126.580				x		
30	Hefei	China	31.825	117.339				x		
31	Heze	China	35.241	115.455	x			x		
32	Hohhot	China	40.701	111.510	x					
33	Huixian	China	35.432	113.771	x					
34	Hulunbuir City	China	49.344	119.661	x	x				
35	Jiaocheng County	China	37.526	112.190	x	x				
36	Jincheng	China	35.701	112.813	x		x			
37	Jinhua	China	29.057	119.558				x		
38	Jinjie Park	China	38.707	110.173	x	x				
39	Jungar Qi	China	40.040	111.270	x					
40	Kaifeng	China	34.744	114.411	x					
41	Kaiyuan	China	23.730	103.195	x					
42	Kuytun/Dushanzi	China	44.352	84.873	x					
43	Lanzhou	China	36.089	103.770	x			x		

Table A1
Continued

	Name	Country	Lat	Lon	Ch	Co	Me	Ur	Ph	Un
44	Leshan	China	29.459	103.784	x					
45	Linyi	China	35.155	118.204						x
46	Linyi	China	35.086	110.749	x					
47	Liuzhou	China	24.358	109.375		x	x	x		
48	Longkou	China	37.637	120.448						x
49	Miaotan Village	China	38.058	108.990						x
50	Nankang	China	25.714	114.790				x		
51	Ningdong base	China	38.197	106.586	x					
52	Qitaihe	China	45.771	130.799	x	x				
53	Quanzhou	China	24.851	118.528				x		
54	Renqiu	China	38.702	116.106	x			x		
55	Shanghai	China	31.162	121.506				x		
56	Shantou	China	23.472	116.713				x		
57	Shaoxing	China	30.087	120.500				x		
58	Shenyang	China	41.821	123.341				x		
59	Shijiazhuang	China	37.978	114.619	x			x		
60	Shizuishan	China	38.929	106.437	x	x				
61	Tengzhou	China	34.971	117.211	x					
62	Tianjin	China	39.115	117.124				x		
63	Urumqi	China	44.032	87.702	x	x				
64	Wenzhou	China	27.876	120.758				x		
65	Wujiang District	China	30.873	120.654						x
66	Wuyang County	China	33.427	113.624	x					
67	Xiamen	China	24.597	118.121				x		
68	Xi'An	China	34.295	108.837	x			x		
69	Xiaoyi	China	37.098	111.797	x	x				
70	Xifeng County	China	27.164	106.719						x
71	Xingping	China	34.292	108.481	x					
72	Xinxiang	China	35.215	113.785	x					
73	Xuzhou	China	34.258	117.223				x		
74	Yichang	China	30.509	111.468	x					
75	Yinchuan	China	38.457	106.060	x					
76	Yingcheng	China	30.950	113.612	x					
77	Yulin	China	38.120	109.556	x					
78	Zhangjiagang	China	31.828	120.448	x			x		
79	Zhangzhou	China	24.540	117.685				x		
80	Zhengzhou	China	34.734	113.583				x		
81	Zhongwei	China	37.627	105.205	x	x				
82	Zhumadian	China	32.973	114.008	x			x		
83	Zibo	China	36.722	118.025						x
84	Bogota	Colombia	4.614	-74.140				x		
85	Ain Sokhna	Egypt	29.670	32.281	x		x			
86	Cairo	Egypt	30.107	31.233				x		

Table A1

Continued

	Name	Country	Lat	Lon	Ch	Co	Me	Ur	Ph	Un
87	Mansoura	Egypt	31.063	31.373	x					
88	Malabo	Equ. Guinea	3.780	8.712	x					
89	Bremen Harbor	Germany	53.103	8.758			x	x		
90	Ankleshwar	India	21.598	73.015					x	
91	Avashi	India	17.620	73.463	x					
92	Birwadi	India	18.131	73.500	x				x	
93	Jawaharlal Nehru	India	17.659	83.079					x	
94	Khopoli	India	18.827	73.241	x					
95	Kistaipally	India	17.577	78.355					x	
96	Taloja	India	19.134	73.195	x				x	
97	Bontang	Indonesia	0.147	117.468	x					
98	Jakarta	Indonesia	-6.239	106.948				x		
99	Medan	Indonesia	3.617	98.642				x		
100	Palembang	Indonesia	-2.964	104.780	x			x		
101	Surabaya	Indonesia	-7.275	112.679	x			x		
102	Asalouyeh	Iran	27.560	52.542	x					
103	Bojnurd	Iran	37.546	57.509	x					
104	Mamaqan	Iran	37.877	45.928	x					
105	Marvdatsh	Iran	29.846	52.725	x					
106	Tabriz	Iran	38.061	46.221	x			x		
107	Tehran	Iran	35.639	51.350				x		
108	Urmia	Iran	37.376	45.245	x					
109	Asahikawa	Japan	43.760	142.368				x		
110	Hirosaki	Japan	40.639	140.475				x		
111	Nagoya	Japan	35.244	136.864	x		x	x		
112	Osaka	Japan	34.551	135.452	x		x	x		
113	Sapporo	Japan	43.105	141.313				x		
114	Tokyo/Yokohama	Japan	35.760	139.788	x		x	x		
115	Kuala Lumpur	Malaysia	3.074	101.478				x		
116	Kuching	Malaysia	1.548	110.388						x
117	Ciudad Juarez	Mexico	31.662	-106.394				x		
118	Mexico City	Mexico	19.459	-99.105				x		
119	Monterrey	Mexico	25.760	-100.289			x	x		
120	Torreon	Mexico	25.672	-103.456				x		
121	Benin City	Nigeria	6.292	5.620				x		
122	Ibadan	Nigeria	7.397	3.939				x		
123	Lagos	Nigeria	6.559	3.295				x		
124	Port Harcourt	Nigeria	4.772	7.039	x			x		
125	Sohar Port	Oman	24.451	56.610	x					
126	Karachi	Pakistan	24.869	67.310	x				x	
127	Manila	Philippines	14.619	121.081				x		
128	Krasnoyarsk	Russia	56.064	92.954						x
129	Novomoskovsk	Russia	54.063	38.188	x					

Table A1
Continued

	Name	Country	Lat	Lon	Ch	Co	Me	Ur	Ph	Un
130	Salavat	Russia	53.382	55.838	x					
131	St-Petersburg	Russia	59.855	30.399				x		
132	Tolyatti	Russia	53.553	49.596	x					
133	Al Jubail	Saudi Arabia	27.057	49.552	x		x			
134	Jeddah	Saudi Arabia	21.429	39.215						x
135	Riyadh	Saudi Arabia	24.593	46.794				x		
136	Secunda	South Africa	-26.571	29.164	x	x				
137	Daegu	South Korea	35.876	128.526				x		
138	Gunsan/Jeonju	South Korea	35.899	126.896				x		
139	Incheon	South Korea	37.462	126.714	x			x		
140	Kaohsiung City	Taiwan	22.582	120.470	x			x		
141	Taichung City	Taiwan	24.129	120.610				x		
142	Taipei	Taiwan	25.017	121.430				x		
143	Ho Chi Minh City	Thailand	10.883	106.676				x		
144	Augusta	USA	33.457	-81.980	x					
145	Baltimore	USA	39.300	-76.554				x		
146	Boston	USA	42.371	-71.148				x		
147	Columbus	USA	39.963	-83.007				x		
148	Detroit	USA	42.334	-83.296				x		
149	Kingsport	USA	36.491	-82.491	x					
150	New York	USA	40.734	-73.973	x			x		
151	Norfolk	USA	36.805	-76.240				x		
152	Philadelphia	USA	39.926	-75.168	x			x		
153	Pittsburgh	USA	40.415	-79.919				x		
154	Fergana	Uzbekistan	40.440	71.847	x			x		
155	Navoi	Uzbekistan	40.077	65.322	x					
156	Tashkent	Uzbekistan	41.288	69.235				x		
157	Barcelona	Venezuela	10.075	-64.772	x					

Note. The categories are abbreviated as Ch for the chemical and petrochemical industry, Co for the coal-related industry, Me for metallurgy, Ur for urban, Ph for the pharmaceutical industry, and Un for undetermined.

Table A2
A Catalog of C₂H₂ Point Sources, With Identified Potential Emitters

	Name	Country	Lat	Lon	Ch	Co	Me	Ur	Ph	Un
1	Baotou	China	40.612	109.735	x	x	x			
2	Changzhi	China	36.467	113.008	x	x				
3	Dalad Banner	China	40.359	109.972	x	x				
4	Datong County	China	36.871	101.747	x	x	x			
5	Hohhot	China	40.737	111.428	x					
6	Huangzhong District	China	36.492	101.535	x	x				
7	Jinjie Park	China	38.703	110.186	x	x				
8	Mengxi Park	China	39.912	106.800	x	x				
9	Shihezi	China	44.361	86.032	x	x	x			
10	Shizuishan	China	38.940	106.429	x	x	x			
11	Urumqi	China	44.008	87.737	x	x				
12	Wuhai	China	39.372	106.726	x	x	x			
13	Xiliangcun	China	41.040	112.125		x				
14	Xining	China	36.639	101.692	x		x			
15	Yushe County	China	37.015	112.899	x	x				
16	Zhangjiakou	China	40.747	114.923	x	x				

Note. The categories are abbreviated as Ch for the chemical and petrochemical industry, Co for the coal-related industry, Me for metallurgy, Ur for urban, Ph for the pharmaceutical industry, and Un for undetermined.

Table A3
A Catalog of C₃H₆ Point Sources, With Identified Potential Emitters

	Name	Country	Lat	Lon	Ch	Co	Me	Ur	Ph	Un
1	Fangshan District	China	39.732	115.905	x					
2	Ningdong base	China	38.181	106.621	x	x				
3	Rabigh	Saudi Arabia	22.701	39.019	x					
4	Secunda	South Africa	-26.564	29.168	x	x				

Note. The categories are abbreviated as Ch for the chemical and petrochemical industry, Co for the coal-related industry, Me for metallurgy, Ur for urban, Ph for the pharmaceutical industry, and Un for undetermined.

Data Availability Statement

The supersampled IASI distributions of CH₃OH, C₂H₂, C₃H₆, and SO₂ generated and analyzed in this study (Franco, Clarisse, & Coheur, 2024) have been deposited in the Zenodo database (<https://doi.org/10.5281/zenodo.12723194>). The supersampled IASI C₂H₄ HRI data set (Franco et al., 2022a) is available from the Zenodo database (<https://doi.org/10.5281/zenodo.7085725>). The IASI NH₃ VCD product can be obtained from the AERIS data infrastructure: IASI/Metop-A (<https://doi.org/10.25326/12>; Clarisse, Van Damme et al., 2023a), IASI/Metop-B (<https://doi.org/10.25326/13>; Clarisse, Van Damme et al., 2023b), and IASI/Metop-C (<https://doi.org/10.25326/500>; Clarisse, Van Damme et al., 2023c). The codes of the oversampling, wind rotation, and supersampling used in this work (Clarisse, Van Damme et al., 2019a) are available at <https://squares.ulb.be/NH3-IASI.html>.

Acknowledgments

This research has been supported by the World Emission project (<https://www.world-emission.com/>) funded by the European Space Agency (contract No. 4000137291/22/I-EF). Activities at ULB have also been supported by the HIRS Prodex arrangement (ESA-BELSP0) and the Spheres project funded under the Actions de Recherche Concertées (ARC) from the French Community (Belgium). L.C. is research associate supported by the F.R.S.–FNRS. The French scientists are grateful to CNES and Centre National de la Recherche Scientifique (CNRS) for financial support. The authors thank Raphaëlle De Cruyenaere for the preliminary analysis of the IASI data in the framework of her master's thesis.

References

Amghizar, I., Vandewalle, L. A., Van Geem, K. M., & Marin, G. B. (2017). New trends in olefin production. *Engineering*, 3(2), 171–178. <https://doi.org/10.1016/J.ENG.2017.02.006>

Atkinson, R. (2007). Gas-phase tropospheric chemistry of organic compounds: A review. *Atmospheric Environment*, 41, 200–240. <https://doi.org/10.1016/j.atmosenv.2007.10.068>

Atkinson, R., & Arey, J. (2003). Atmospheric degradation of volatile organic compounds. *Chemical Reviews*, 103(12), 4605–4638. <https://doi.org/10.1021/cr0206420>

Barkley, M. P., González Abad, G., Kurosu, T. P., Spurr, R., Torbatian, S., & Lerot, C. (2017). OMI air-quality monitoring over the Middle East. *Atmospheric Chemistry and Physics*, 17(7), 4687–4709. <https://doi.org/10.5194/acp-17-4687-2017>

Bates, K. H., Jacob, D. J., Wang, S., Hornbrook, R. S., Apel, E. C., Kim, M. J., et al. (2021). The global budget of atmospheric methanol: New constraints on secondary, oceanic, and terrestrial sources. *Journal of Geophysical Research: Atmospheres*, 126(4), e2020JD033439. <https://doi.org/10.1029/2020jd033439>

Beirle, S., Boersma, K. F., Platt, U., Lawrence, M. G., & Wagner, T. (2011). Megacity emissions and lifetimes of nitrogen oxides probed from space. *Science*, 333(6050), 1737–1739. <https://doi.org/10.1126/science.1207824>

Beirle, S., Borger, C., Jost, A., & Wagner, T. (2023). Improved catalog of NH_x point source emissions (version 2). *Earth System Science Data*, 15(7), 3051–3073. <https://doi.org/10.5194/essd-15-3051-2023>

Bernath, P. F., Steffen, J., Crouse, J., & Boone, C. D. (2020). Sixteen-year trends in atmospheric trace gases from orbit. *Journal of Quantitative Spectroscopy and Radiative Transfer*, 253, 107178. <https://doi.org/10.1016/j.jqsrt.2020.107178>

Bouillon, M., Safieddine, S., Hadji-Lazaro, J., Whitburn, S., Clarisse, L., Doutriaux-Boucher, M., et al. (2020). Ten-Year assessment of IASI radiance and temperature. *Remote Sensing*, 12(15), 2393. <https://doi.org/10.3390/rs12152393>

Cady-Pereira, K. E., Shephard, M. W., Millet, D. B., Luo, M., Wells, K. C., Xiao, Y., et al. (2012). Methanol from TES global observations: Retrieval algorithm and seasonal and spatial variability. *Atmospheric Chemistry and Physics*, 12(17), 8189–8203. <https://doi.org/10.5194/acp-12-8189-2012>

Cho, C., St. Clair, J. M., Liao, J., Wolfe, G. M., Jeong, S., il Kang, D., et al. (2021). Evolution of formaldehyde (HCHO) in a plume originating from a petrochemical industry and its volatile organic compounds (VOCs) emission rate estimation. *Elementa: Science of the Anthropocene*, 9(1), 00015. <https://doi.org/10.1525/elementa.2021.00015>

Clarisse, L., Clerbaux, C., Franco, B., Hadji-Lazaro, J., Whitburn, S., Kopp, A. K., et al. (2019). A decadal data set of global atmospheric dust retrieved from IASI satellite measurements. *Journal of Geophysical Research: Atmospheres*, 124(3), 1618–1647. <https://doi.org/10.1029/2018jd029701>

Clarisse, L., Coheur, P.-F., Prata, F., Hadji-Lazaro, J., Hurtmans, D., & Clerbaux, C. (2013). A unified approach to infrared aerosol remote sensing and type specification. *Atmospheric Chemistry and Physics*, 13(4), 2195–2221. <https://doi.org/10.5194/acp-13-2195-2013>

Clarisse, L., Franco, B., Van Damme, M., Di Gioacchino, T., Hadji-Lazaro, J., Whitburn, S., et al. (2023). The IASI NH₃ version 4 product: Averaging kernels and improved consistency. *Atmospheric Measurement Techniques*, 16(21), 5009–5028. <https://doi.org/10.5194/amt-16-5009-2023>

Clarisse, L., Fromm, M., Ngadi, Y., Emmons, L., Clerbaux, C., Hurtmans, D., & Coheur, P.-F. (2011a). Intercontinental transport of anthropogenic sulfur dioxide and other pollutants: An infrared remote sensing case study. *Geophysical Research Letters*, 38(19), L19806. <https://doi.org/10.1029/2011gl048976>

Clarisse, L., R'Honi, Y., Coheur, P.-F., Hurtmans, D., & Clerbaux, C. (2011b). Thermal infrared nadir observations of 24 atmospheric gases. *Geophysical Research Letters*, 38(10), L10802. <https://doi.org/10.1029/2011gl047271>

Clarisse, L., Van Damme, M., Clerbaux, C., & Coheur, P.-F. (2019a). Oversampling, wind-rotation, and supersampling codes [Software]. <https://squares.ulb.be/NH3-IASI.html>

Clarisse, L., Van Damme, M., Clerbaux, C., & Coheur, P.-F. (2019b). Tracking down global NH₃ point sources with wind-adjusted super-resolution. *Atmospheric Measurement Techniques*, 12(10), 5457–5473. <https://doi.org/10.5194/amt-12-5457-2019>

Clarisse, L., Van Damme, M., Clerbaux, C., & Coheur, P.-F. (2023a). Reanalyzed daily IASI/Metop-A ULB-LATMOS ammonia (NH₃) L2 product (total column) [Dataset]. *AERIS*. <https://doi.org/10.25326/12>

Clarisse, L., Van Damme, M., Clerbaux, C., & Coheur, P.-F. (2023b). Reanalyzed daily IASI/Metop-B ULB-LATMOS ammonia (NH₃) L2 product (total column) [Dataset]. *AERIS*. <https://doi.org/10.25326/13>

Clarisse, L., Van Damme, M., Clerbaux, C., & Coheur, P.-F. (2023c). Reanalyzed daily IASI/Metop-C ULB-LATMOS ammonia (NH₃) L2 product (total column) [Dataset]. *AERIS*. <https://doi.org/10.25326/500>

Clerbaux, C., Boynard, A., Clarisse, L., George, M., Hadji-Lazaro, J., Herbin, H., et al. (2009). Monitoring of atmospheric composition using the thermal infrared IASI/MetOp sounder. *Atmospheric Chemistry and Physics*, 9(16), 6041–6054. <https://doi.org/10.5194/acp-9-6041-2009>

Crelling, J. C., Hagemann, H. W., Sauter, D. H., Ramani, R. V., Vogt, W., Leininger, D., et al. (2010). Coal. In *Ullmann's encyclopedia of industrial chemistry*. John Wiley and Sons, Ltd. https://doi.org/10.1002/14356007.a07_153.pub4

de Gouw, J. A., Gilman, J. B., Kim, S., Alvarez, S. L., Dusanter, S., Graus, M., et al. (2018). Chemistry of volatile organic compounds in the Los Angeles basin: Formation of oxygenated compounds and determination of emission ratios. *Journal of Geophysical Research: Atmospheres*, 123(4), 2298–2319. <https://doi.org/10.1002/2017jd027976>

de Gouw, J. A., Middlebrook, A. M., Warneke, C., Goldan, P. D., Kuster, W. C., Roberts, J. M., et al. (2005). Budget of organic carbon in a polluted atmosphere: Results from the new england air quality study in 2002. *Journal of Geophysical Research*, 110(D16). <https://doi.org/10.1029/2004jd005623>

De Longueville, H., Clarisse, L., Whitburn, S., Franco, B., Bauduin, S., Clerbaux, C., et al. (2021). Identification of short and long-lived atmospheric trace gases from IASI space observations. *Geophysical Research Letters*, 48(5), e2020GL091742. <https://doi.org/10.1029/2020gl091742>

Di Gioacchino, T., Clarisse, L., Noppen, L., Van Damme, M., Bauduin, S., & Coheur, P. (2024). Spatial and temporal variations of thermal contrast in the planetary boundary layer. *Journal of Remote Sensing*, 28, 0142. <https://doi.org/10.34133/remotesensing.0142>

Duflo, V., Wespes, C., Clarisse, L., Hurtmans, D., Ngadi, Y., Jones, N., et al. (2015). Acetylene (C₂H₂) and hydrogen cyanide (HCN) from IASI satellite observations: Global distributions, validation, and comparison with model. *Atmospheric Chemistry and Physics*, 15(18), 10509–10527. <https://doi.org/10.5194/acp-15-10509-2015>

Fioletov, V. E., McLinden, C. A., Griffin, D., Abboud, I., Krotkov, N., Leonard, P. J. T., et al. (2023). Version 2 of the global catalogue of large anthropogenic and volcanic SO₂ sources and emissions derived from satellite measurements. *Earth System Science Data*, 15(1), 75–93. <https://doi.org/10.5194/essd-15-75-2023>

- Fioletov, V. E., McLinden, C. A., Krotkov, N., Yang, K., Loyola, D. G., Valks, P., et al. (2013). Application of OMI, SCIAMACHY, and GOME-2 satellite SO₂ retrievals for detection of large emission sources. *Journal of Geophysical Research: Atmospheres*, *118*(19), 11–399. <https://doi.org/10.1002/jgrd.50826>
- Franco, B., Clarisse, L., & Coheur, P. (2024a). Methanol (CH₃OH), acetylene (C₂H₂), and propylene (C₃H₆) point-sources detected by the IASI infrared satellite instrument (2007–2023) [Dataset]. *Zenodo*. <https://doi.org/10.5281/ZENODO.12723194>
- Franco, B., Clarisse, L., Stavrou, T., Müller, J.-F., Van Damme, M., Whitburn, S., et al. (2018). A general framework for global retrievals of trace gases from IASI: Application to methanol, formic acid, and PAN. *Journal of Geophysical Research: Atmospheres*, *123*(24), 13963–13984. <https://doi.org/10.1029/2018jd029633>
- Franco, B., Clarisse, L., Theys, N., Hadji-Lazaro, J., Clerbaux, C., & Coheur, P. (2024b). Pyrogenic HONO seen from space: Insights from global IASI observations. *Atmospheric Chemistry and Physics*, *24*(8), 4973–5007. <https://doi.org/10.5194/acp-24-4973-2024>
- Franco, B., Clarisse, L., Van Damme, M., Hadji-Lazaro, J., Clerbaux, C., & Coheur, P. (2022a). Ethylene (C₂H₄) point-sources detected by the IASI infrared satellite instrument (2008–2020) [Dataset]. *Zenodo*. <https://doi.org/10.5281/ZENODO.7085724>
- Franco, B., Clarisse, L., Van Damme, M., Hadji-Lazaro, J., Clerbaux, C., & Coheur, P.-F. (2022b). Ethylene industrial emitters seen from space. *Nature Communications*, *13*(1), 6452. <https://doi.org/10.1038/s41467-022-34098-8>
- Fried, A., Walega, J., Weibring, P., Richter, D., Simpson, I. J., Blake, D. R., et al. (2020). Airborne formaldehyde and volatile organic compound measurements over the Daesan petrochemical complex on Korea's northwest coast during the Korea-United States Air Quality study: Estimation of emission fluxes and effects on air quality. *Elementa: Science of the Anthropocene*, *8*(1), 121. <https://doi.org/10.1525/elementa.2020.121>
- Heald, C. L., & Kroll, J. H. (2020). The fuel of atmospheric chemistry: Toward a complete description of reactive organic carbon. *Science Advances*, *6*(6), eaay8967. <https://doi.org/10.1126/sciadv.aay8967>
- Hersbach, H., Bell, B., Berrisford, P., Hirahara, S., Horányi, A., Muñoz-Sabater, J., et al. (2020). The ERA5 global reanalysis. *Quarterly Journal of the Royal Meteorological Society*, *146*(730), 1999–2049. <https://doi.org/10.1002/qj.3803>
- Jacob, D. J., Field, B. D., Li, Q., Blake, D. R., de Gouw, J., Warneke, C., et al. (2005). Global budget of methanol: Constraints from atmospheric observations. *Journal of Geophysical Research*, *110*(D8). <https://doi.org/10.1029/2004jd005172>
- Khan, M. A. H., Cooke, M. C., Utembe, S. R., Xiao, P., Derwent, R. G., Jenkin, M. E., et al. (2014). Reassessing the photochemical production of methanol from peroxy radical self and cross reactions using the STOCHEM-CRI global chemistry and transport model. *Atmospheric Environment*, *99*, 77–84. <https://doi.org/10.1016/j.atmosenv.2014.09.056>
- Lauvaux, T., Giron, C., Mazzolini, M., d'Aspremont, A., Duren, R., Cusworth, D., et al. (2022). Global assessment of oil and gas methane ultra-emitters. *Science*, *375*(6580), 557–561. <https://doi.org/10.1126/science.abj4351>
- Lerot, C., Hendrick, F., Van Roozendaal, M., Alvarado, L. M. A., Richter, A., De Smedt, I., et al. (2021). Glyoxal tropospheric column retrievals from TROPOMI - Multi-satellite intercomparison and ground-based validation. *Atmospheric Measurement Techniques*, *14*(12), 7775–7807. <https://doi.org/10.5194/amt-14-7775-2021>
- Li, M., Patino-Echeverri, D., & Zhang, J. J. (2019). Policies to promote energy efficiency and air emissions reductions in China's electric power generation sector during the 11th and 12th five-year plan periods: Achievements, remaining challenges, and opportunities. *Energy Policy*, *125*, 429–444. <https://doi.org/10.1016/j.enpol.2018.10.008>
- Liu, F., Choi, S., Li, C., Fioletov, V. E., McLinden, C. A., Joiner, J., et al. (2018). A new global anthropogenic SO₂ emission inventory for the last decade: A mosaic of satellite-derived and bottom-up emissions. *Atmospheric Chemistry and Physics*, *18*(22), 16571–16586. <https://doi.org/10.5194/acp-18-16571-2018>
- McLinden, C. A., Fioletov, V., Shephard, M. W., Krotkov, N., Li, C., Martin, R. V., et al. (2016). Space-based detection of missing sulfur dioxide sources of global air pollution. *Nature Geoscience*, *9*(7), 496–500. <https://doi.org/10.1038/ngeo2724>
- Millet, D. B., Jacob, D. J., Custer, T. G., de Gouw, J. A., Goldstein, A. H., Karl, T., et al. (2008). New constraints on terrestrial and oceanic sources of atmospheric methanol. *Atmospheric Chemistry and Physics*, *8*(23), 6887–6905. <https://doi.org/10.5194/acp-8-6887-2008>
- Müller, J.-F., Liu, Z., Nguyen, V. S., Stavrou, T., Harvey, J. N., & Peeters, J. (2016). The reaction of methyl peroxy and hydroxyl radicals as a major source of atmospheric methanol. *Nature Communications*, *7*(1), 13213. <https://doi.org/10.1038/ncomms13213>
- Ott, J., Gronemann, V., Pontzen, F., Fiedler, E., Grossmann, G., Kersebohm, D. B., et al. (2012). Methanol. In *Ullmann's encyclopedia of industrial chemistry*. John Wiley and Sons, Ltd. https://doi.org/10.1002/14356007.a16_465.pub3
- Parrish, D. D., Ryerson, T. B., Mellqvist, J., Johansson, J., Fried, A., Richter, D., et al. (2012). Primary and secondary sources of formaldehyde in urban atmospheres: Houston Texas region. *Atmospheric Chemistry and Physics*, *12*(7), 3273–3288. <https://doi.org/10.5194/acp-12-3273-2012>
- Pässler, P., Hefner, W., Buckl, K., Meinass, H., Meiswinkel, A., Wernicke, H.-J., et al. (2011). Acetylene. In *Ullmann's encyclopedia of industrial chemistry*. John Wiley and Sons, Ltd. https://doi.org/10.1002/14356007.a01_097.pub4
- Ryerson, T. B., Trainer, M., Angevine, W. M., Brock, C. A., Dissly, R. W., Fehsenfeld, F. C., et al. (2003). Effect of petrochemical industrial emissions of reactive alkenes and NO_x tropospheric ozone formation in Houston, Texas. *Journal of Geophysical Research*, *108*(D8). <https://doi.org/10.1029/2002jd003070>
- Saunders, R. W., Blackmore, T. A., Candy, B., Francis, P. N., & Hewison, T. J. (2021). Ten years of satellite infrared radiance monitoring with the met office NWP model. *IEEE Transactions on Geoscience and Remote Sensing*, *59*(6), 4561–4569. <https://doi.org/10.1109/tgrs.2020.3015257>
- Seinfeld, J. H., & Pandis, S. N. (2016). *Atmospheric chemistry and physics: From air pollution to climate change*. John Wiley and Sons.
- Simpson, I. J., Blake, D. R., Blake, N. J., Meinardi, S., Barletta, B., Hughes, S. C., et al. (2020). Characterization, sources and reactivity of volatile organic compounds (VOCs) in Seoul and surrounding regions during KORUS-AQ. *Elementa: Science of the Anthropocene*, *8*, 37. <https://doi.org/10.1525/elementa.434>
- Sun, K., Zhu, L., Cady-Pereira, K., Miller, C. C., Chance, K., Clarisse, L., et al. (2018). A physics-based approach to oversample multi-satellite, multispecies observations to a common grid. *Atmospheric Measurement Techniques*, *11*(12), 6679–6701. <https://doi.org/10.5194/amt-11-6679-2018>
- Theys, N., Fioletov, V., Li, C., De Smedt, I., Lerot, C., McLinden, C., et al. (2021). A sulfur dioxide covariance-based retrieval algorithm (COBRA): Application to TROPOMI reveals new emission sources. *Atmospheric Chemistry and Physics*, *21*(22), 16727–16744. <https://doi.org/10.5194/acp-21-16727-2021>
- Tong, D., Zhang, Q., Liu, F., Geng, G., Zheng, Y., Xue, T., et al. (2018). Current emissions and future mitigation pathways of coal-fired power plants in China from 2010 to 2030. *Environmental Science & Technology*, *52*(21), 12905–12914. <https://doi.org/10.1021/acs.est.8b02919>
- Valin, L. C., Russell, A. R., & Cohen, R. C. (2013). Variations of OH radical in an urban plume inferred from NO₂ column measurements. *Geophysical Research Letters*, *40*(9), 1856–1860. <https://doi.org/10.1002/grl.50267>
- Van Damme, M., Clarisse, L., Whitburn, S., Hadji-Lazaro, J., Hurtmans, D., Clerbaux, C., & Coheur, P.-F. (2018). Industrial and agricultural ammonia point sources exposed. *Nature*, *564*(7734), 99–103. <https://doi.org/10.1038/s41586-018-0747-1>

- Volkamer, R., Jimenez, J. L., San Martini, F., Dzepina, K., Zhang, Q., Salcedo, D., et al. (2006). Secondary organic aerosol formation from anthropogenic air pollution: Rapid and higher than expected. *Geophysical Research Letters*, *33*(17). <https://doi.org/10.1029/2006gl026899>
- Volkamer, R., Ziemann, P. J., & Molina, M. J. (2009). Secondary organic aerosol formation from acetylene (C₂H₂): Seed effect on SOA yields due to organic photochemistry in the aerosol aqueous phase. *Atmospheric Chemistry and Physics*, *9*(6), 1907–1928. <https://doi.org/10.5194/acp-9-1907-2009>
- Walker, J. C., Dudhia, A., & Carboni, E. (2011). An effective method for the detection of trace species demonstrated using the MetOp Infrared Atmospheric Sounding Interferometer. *Atmospheric Measurement Techniques*, *4*(8), 1567–1580. <https://doi.org/10.5194/amt-4-1567-2011>
- Wells, K. C., Millet, D. B., Hu, L., Cady-Pereira, K. E., Xiao, Y., Shephard, M. W., et al. (2012). Tropospheric methanol observations from space: Retrieval evaluation and constraints on the seasonality of biogenic emissions. *Atmospheric Chemistry and Physics*, *12*(13), 5897–5912. <https://doi.org/10.5194/acp-12-5897-2012>
- Wert, B. P., Trainer, M., Fried, A., Ryerson, T. B., Henry, B., Potter, W., et al. (2003). Signatures of terminal alkene oxidation in airborne formaldehyde measurements during TexAQ5 2000. *Journal of Geophysical Research*, *108*(D3), 4104. <https://doi.org/10.1029/2002JD002502>
- Whitburn, S., Van Damme, M., Clarisse, L., Bauduin, S., Heald, C. L., Hadji-Lazaro, J., et al. (2016). A flexible and robust neural network IASI-NH₃ retrieval algorithm. *Journal of Geophysical Research: Atmospheres*, *121*(11), 6581–6599. <https://doi.org/10.1002/2016jd024828>
- Xiao, Y., Jacob, D. J., & Turquety, S. (2007). Atmospheric acetylene and its relationship with CO as an indicator of air mass age. *Journal of Geophysical Research*, *112*(D12). <https://doi.org/10.1029/2006jd008268>
- Yang, C.-J. (2015). U.S. Shale gas versus China's coal as chemical feedstock. *Environmental Science & Technology*, *49*(16), 9501–9502. <https://doi.org/10.1021/acs.est.5b03562>
- Zhou, D. K., Larar, A. M., Liu, X., Smith, W. L., Strow, L. L., Yang, P., et al. (2011). Global land surface emissivity retrieved from satellite ultraviolet IR measurements. *IEEE Transactions on Geoscience and Remote Sensing*, *49*(4), 1277–1290. <https://doi.org/10.1109/tgrs.2010.2051036>
- Zhu, L., Jacob, D. J., Mickley, L. J., Marais, E. A., Cohan, D. S., Yoshida, Y., et al. (2014). Anthropogenic emissions of highly reactive volatile organic compounds in eastern Texas inferred from oversampling of satellite (OMI) measurements of HCHO columns. *Environmental Research Letters*, *9*(11), 114004. <https://doi.org/10.1088/1748-9326/9/11/114004>
- Zimmermann, H. (2013). Propene. In *Ullmann's encyclopedia of industrial chemistry*. John Wiley and Sons, Ltd. https://doi.org/10.1002/14356007.a22_211.pub3
- Zimmermann, H., & Walzl, R. (2009). Ethylene. In *Ullmann's encyclopedia of industrial chemistry*. John Wiley and Sons, Ltd. https://doi.org/10.1002/14356007.a10_045.pub3
- Zuo, X., Sun, W., De Smedt, I., Li, X., Liu, S., Pu, D., et al. (2023). Observing downwind structures of urban HCHO plumes from space: Implications to non-methane volatile organic compound emissions. *Geophysical Research Letters*, *50*(24), e2023GL106062. <https://doi.org/10.1029/2023gl106062>